POLITECNICO DI TORINO
Repository ISTITUZIONALE

Influence of Friction Stir Welding and Post-Weld Aging on Corrosion Behavior of LPBF A20X Alloy

Original
Influence of Friction Stir Welding and Post-Weld Aging on Corrosion Behavior of LPBF A20X Alloy / Abankar, M., Matteis, P., Russo Spena, P.. - In: METALS. - ISSN 2075-4701. - 16:10(2026). [10.3390/met16101092]

Availability:
This version is available at: 11583/3016568 since: 2026-10-12T12:29:47Z

Publisher:
Metals

Published
DOI:10.3390/met16101092

Terms of use:

This article is made available under terms and conditions as specified in the corresponding bibliographic description in the repository

Publisher copyright

(Article begins on next page)

18 November 2026

metals

Article

Influence of Friction Stir Welding and Post-Weld Aging on Corrosion Behavior of LPBF A20X Alloy

Mohammad Abankar [1,2], Paolo Matteis [3] and Pasquale Russo Spena [1,2,*]

[1] Department of Management and Production Engineering, Politecnico di Torino, Corso Duca degli Abruzzi 24, 10129 Torino, Italy; mohammad.abankar@polito.it
[2] Advanced Joining Technologies Center J–Tech@PoliTO, Politecnico di Torino, Corso Duca degli Abruzzi 24, 10129 Torino, Italy
[3] Department of Applied Science and Technology, Politecnico di Torino, Corso Duca degli Abruzzi 24, 10129 Torino, Italy; paolo.matteis@polito.it
* Correspondence: pasquale.russospena@polito.it; Tel.: +39-0110907298

Abstract

Laser powder bed fusion (LPBF) enables the production of high-strength A20X aluminum components with complex geometries for aerospace applications. However, the limited build volume of LPBF systems often requires separately manufactured parts to be joined. This study compares the microstructure and corrosion behavior of LPBF A20X under four material conditions: base material (BM), as-welded stir zone (SZ), solution-treated and peak-aged base material (BM–PA), and solution-treated and peak-aged stir zone (SZ–PA). Microstructural evolution was assessed using electron microscopy and X-ray diffraction, while corrosion behavior was evaluated by electrochemical impedance spectroscopy and potentiodynamic polarization in 3.5 wt.% NaCl solution. Among the tested specimens, BM exhibited the lowest corrosion current density (0.703 μA/cm^2), followed by SZ (0.966 μA/cm^2), BM–PA (2.257 μA/cm^2), and SZ–PA (3.181 μA/cm^2). The impedance response and post-polarization SEM observations indicated lower corrosion resistance after solution treatment and aging, particularly in SZ–PA. These findings are consistent with a possible contribution from micro-galvanic interactions involving redistributed and precipitated Cu-rich constituents, TiB_2 particles, and the Al matrix. Under the tested conditions, post-weld heat treatment reduced corrosion resistance compared to FSW alone. This underlines the need to optimize welding and heat-treatment parameters for LPBF A20X components.

Keywords: friction stir welding; A20X; laser powder bed fusion; post-weld aging; electrochemical impedance spectroscopy; pitting corrosion

Academic Editor: Yufeng Sun

Received: 29 August 2026
Revised: 29 September 2026
Accepted: 30 September 2026
Published: 2 October 2026

Copyright: © 2026 by the authors. Licensee MDPI, Basel, Switzerland. This article is an open access article distributed under the terms and conditions of the Creative Commons Attribution (CC BY) license.

1. Introduction

Additive manufacturing has attracted considerable attention because it enables the production of complex geometries that are difficult or impossible to obtain using conventional manufacturing routes. Among the aluminum alloys processed by laser powder bed fusion (LPBF), A20X has emerged as a promising material because it combines the design freedom of additive manufacturing with high specific strength and good thermal stability [1–4]. The alloy was developed primarily for aerospace applications, where low density and high mechanical performance are required [5]. The high strength of A20X results from the combination of its fine LPBF microstructure and

the dispersion of strengthening phases within the Al matrix [6]. In the as-built state, A20X typically exhibits an equiaxed grain structure with an average grain size of 0.5–2 μm and no pronounced crystallographic texture [7–10]. Because A20X is precipitation-hardenable, several studies have examined the effects of post-build heat treatments [3,10–13]. Avateffazeli et al. [10] and Shakil et al. [13] proposed multistep solution treatments followed by T6 aging to improve the microstructure and tensile properties of LPBF A20X. Barode et al. [11] investigated a shorter single-step solution treatment followed by T6 aging. In the peak-aged T6 conditions, these studies reported grain sizes of 2–5 μm, ultimate tensile strengths of 435–483 MPa, and elongations at fracture of 9.5–10.6%, with strengthening mainly associated with the precipitation of θ′- and Ω–Al_2Cu phases [10].

Interest in additively manufactured A20X continues to grow in sectors requiring lightweight structural components. However, the relatively small build chambers of LPBF systems limit the dimensions of the components that can be produced, and separately manufactured parts may therefore need to be joined. Joining LPBF-produced components represents an attractive approach for fabricating larger structures and integrating similar or dissimilar materials, motivating studies on the weldability of additively manufactured alloys [14–19]. Friction stir welding (FSW) is particularly attractive for high-strength aluminum alloys because it is a solid-state process and usually provides joints with better mechanical performance than conventional fusion welding [20–22]. These advantages are commonly linked to grain refinement in the weld region and to the mitigation of solidification defects commonly associated with fusion welding, such as cracking, chemical segregation, and gas porosity [18,23–25]. Scherillo et al. [26] showed that FSW of as-printed AlSi10Mg disrupted the layer-by-layer microstructure, refined the grains through recrystallization, and reduced the porosity inherited from additive manufacturing. Mirandola et al. [27] demonstrated the feasibility of butt FSW in LPBF Scalmalloy® plates and found that build direction had no measurable effect on processability or on the resulting microstructural and mechanical properties. For LPBF A20X, Abankar et al. [14] identified a welding speed of 100 mm/min and a rotational speed of 1500 rpm as suitable parameters for producing a defect-free joint with satisfactory mechanical performance. Under these conditions, the stir zone exhibited a fine recrystallized microstructure with a grain size comparable to that of the LPBF base material, indicating that FSW can preserve substantial microstructural homogeneity across the joint. In a previous study by the present authors [28], the effects of post-weld heat treatment on the microstructure and mechanical properties of both as-built A20X and FSW joints were examined. A solution treatment at 530 °C for 2.5 h followed by aging at 195 °C for 8 h was identified as the condition producing peak hardness.

Several researchers have also investigated the influence of FSW on the corrosion behavior of aluminum alloys, showing that the resulting response depends strongly on alloy composition, precipitate distribution, initial temper, and welding condition [29–33]. Kureshi et al. [33] reported improved corrosion resistance in FSW 7004 aluminum alloy joints compared with gas tungsten arc welding (GTAW) and gas metal arc welding (GMAW) processes, mainly because of the finer and more homogeneous weld microstructure. Fahimpour et al. [34] observed that FSW joints in Al6061 exhibited better corrosion performance than GTAW joints, although the weld zones produced by both processes remained less corrosion-resistant than the base metal. They also reported that a T6 heat treatment improved corrosion behavior, particularly in the weld region. In contrast, Gharavi et al. [35] found that FSW of AA6061–T6 lap joints reduced corrosion resistance because the redistribution of intermetallic particles generated additional galvanic couples. Cu-rich precipitates are particularly relevant in this regard: Wei et al. [36] showed that these precipitates can promote galvanic activity at the precipitate/matrix interface, thereby increasing susceptibility to localized corrosion. Similarly, Adjei-

Kyeremeh et al. [37] found that the enhanced formation of Cu-rich precipitates at higher preheating temperatures in LPBF AA2099 was accompanied by increased corrosion current density and corrosion rate. These contrasting findings indicate that the influence of FSW and heat treatment on corrosion resistance is alloy- and microstructure-dependent.

Despite these advances, the combined effects of FSW and a post-weld heat treatment comprising solution treatment and peak-aging on the electrochemical behavior of LPBF A20X have not been systematically investigated. In particular, the relationship between the redistribution and precipitation of Cu-rich constituents during welding and heat treatment and the resulting electrochemical response remains insufficiently understood. Aluminum alloys normally develop a protective surface film composed primarily of aluminum oxide and hydroxide species [38]. In chloride-containing environments, however, chloride ions can promote localized breakdown of this film and the initiation of pitting corrosion, thereby reducing the service life of the material [39,40]. The present study therefore compares the LPBF base material and the FSW stir zone under the selected as-welded and peak-aged conditions. Microstructural and phase evolution are correlated with electrochemical impedance spectroscopy, potentiodynamic polarization, and post-polarization SEM/EDS observations. The objective is to determine the respective effects of FSW and post-weld heat treatment on corrosion behavior and to assess whether the observed electrochemical trends are consistent with changes in the morphology and distribution of Cu-rich constituents.

2. Materials and Methods

2.1. Additive Manufacturing

LPBF was used to fabricate 75 × 55 × 4 mm A20X plates with the 75 mm dimension oriented parallel to the build direction. These plates were produced by a contract manufacturer (Beamit S.p.A., Reggio Emilia, Italy) using a proprietary LPBF parameter set, representative of current state-of-the-art processing conditions for this alloy. According to the supplier's technical datasheet, the A20X powder consisted of particles ranging in size from 20 to 63 μm, with the chemical composition listed in Table 1. The LPBF process parameters included a laser power of 370 W, a layer thickness of 30 μm, and an alternating stripe pattern. The as-built A20X plates had an average density of 99.7%, as determined by optical microscopy and X-ray tomography (further details are provided in [14]).

Table 1. Nominal chemical composition of A20X powder, according to the supplier's technical datasheet.

Element	Cu	Si	Mg	B	Ag	Ti	Fe	Al
wt.%	4.2–5.0	0.1 max	0.20–0.33	1.25–1.55	0.6–0.9	3.00–3.85	0.08 max	bal.

2.2. Welding and Heat Treatment

Single-pass friction stir butt welding was performed on A20X plates using an FSW machine (Stirtec GmbH, Graz, Austria) equipped with a water-cooled spindle, with the weld line oriented parallel to the build direction. The FSW tool, made of HS6–5–2–5 high-speed steel [41], featured a shoulder diameter of 12 mm and a 3.8 mm long truncated conical pin with a cone angle of 15°. The pin had a threaded surface to enhance material stirring. The tool had a tilt angle of 2°. To limit surface oxidation and the possible entrainment of oxide particles into the stirred material, argon gas was supplied at a flow rate of 10 L/min through two nozzles positioned at the front and rear of the tool. The following FSW parameters were selected: plunge depth of 3.8 mm, plunge speed of 10

mm/min, dwell time of 2 s, rotational speed of 1500 rpm, and welding speed of 100 mm/min. These welding parameters were selected based on previous work [15] and on a preliminary experimental campaign, with the aim of producing sound joints.

The welded joints were then subjected to post-weld heat treatment consisting of solution treatment at 530 °C for 2.5 h followed by aging at 195 °C for 8 h. Unwelded coupons were subjected to the same thermal cycle to obtain the heat-treated base material condition. These heat-treatment parameters were selected based on a preliminary experimental campaign [28], in which they enabled peak hardness to be achieved. Therefore, this heat-treatment condition is defined here as solution-treated and peak-aged (PA). For clarity, the base material is referred to as BM, the stir zone of the as-welded joint as SZ, the base material subjected to the solution-treatment and aging cycle as BM–PA, and the stir zone sampled from joints subjected to the same post-weld heat treatment as SZ–PA. Under each examined condition, five Vickers indentations were performed on each specimen to characterize the hardness response and identify the most appropriate heat-treatment condition. Hardness indents were performed at the center of the stir zone. The HAZ was not evaluated as a separate corrosion condition because our microstructural observations did not reveal an obvious difference in precipitate distribution between the HAZ and BM. However, subtle HAZ-specific microstructural changes may still influence localized corrosion behavior, even without significant differences in hardness or mechanical properties. Therefore, a dedicated electrochemical investigation of the HAZ is considered an important subject for future work.

2.3. Metallographic and XRD Analyses

Metallographic specimens were prepared using standard grinding and polishing procedures followed by final etching with Keller's reagent. Microstructural observations were carried out by field-emission SEM mod. MIRA3 (TESCAN, Brno, Czech Republic) using a backscattered-electron detector. TEM lamellae were extracted from polished cross-sections using a Xe focused ion beam (FIB) system mod. Solaris X (TESCAN, Brno, Czech Republic) equipped with a micromanipulator, mounted on molybdenum grids, and thinned in the same instrument. High-magnification TEM observations were performed using a TALOS F200X microscope (Thermo Fischer Scientific Inc., Waltham, MA, USA). Scanning TEM in high-angle annular dark-field mode (STEM–HAADF), together with STEM–EDS elemental mapping, was used to analyze the distribution of alloying elements. The crystalline phase in the samples was analyzed by X-ray diffraction (XRD) using a Bourevestnik Dron–8 diffractometer (Bourevestnik JSC, Saint Petersburg, Russia) with Cu Kα radiation (λ = 1.5428 Å).

Vickers microhardness measurements were performed according to ISO 6507–1:2023 [42] using a load of 0.2 kgf and a dwell time of 10 s.

2.4. Electrochemical Testing

Because Rafieazad et al. [43] reported essentially isotropic corrosion behavior for LPBF A20X, the present study focuses on the material condition rather than on build-direction effects. To evaluate the corrosion behavior of the samples, electrochemical impedance spectroscopy (EIS) and potentiodynamic polarization (Tafel analysis) tests were performed in 250 mL of a 3.5 wt.% NaCl solution after 30 min of immersion at room temperature during which the open-circuit potential (OCP) was monitored. Tests were carried out using a conventional three-electrode cell connected to a PARSTAT 2273 potentiostat (Princeton Applied Research, Oak Ridge, TN, USA), with the specimen as the working electrode, a platinum counter electrode, and an Ag/AgCl reference electrode. One electrochemical measurement was performed for each material condition. Because only one electrochemical measurement was obtained for each condition, the reported

values are interpreted as condition-specific comparative observations among the tested conditions. The fixed 30 min immersion period characterizes the short-term response after standardized preconditioning and does not establish long-term passive-film stability or re-passivation behavior.

An exposed area of 4 cm^2 (20 × 20 mm) was defined by masking the remaining surfaces with an insulating lacquer. Before testing, the surfaces were ground with 2500-grit SiC paper, degreased in acetone, rinsed with distilled water, and air-dried. For the additively manufactured specimens, the tested surface was parallel to the build direction. For the welded specimens, the central region of the upper surface parallel to the welding direction was tested.

Before EIS testing, the open-circuit potential was monitored until a stable potential was obtained. EIS measurements were then performed at the OCP using a sinusoidal voltage amplitude of 10 mV over a frequency range of 100 kHz to 10 mHz. Potentiodynamic polarization was subsequently performed on the same specimen from −250 mV vs. the open-circuit potential (OCP) to +600 mV vs. the Ag/AgCl electrode at a scan rate of 1 mV/s, after which the corroded surfaces were examined using SEM and EDS. Corroded surfaces have been examined using a Philips XI30 Scanning Electron Microscope (SEM, Hillsboro, OR, USA). The corrosion current density (I_{corr}), corrosion potential (E_{corr}), and polarization resistance (R_p) were extracted from the polarization curves to assess the corrosion behavior for the different material conditions. The polarization resistance was calculated using the Stern–Geary relationship [32]:

$$R_p = (\beta a \cdot \beta c) / (2.303 \cdot (\beta a + \beta c) \cdot I_{cor}), \quad (1)$$

where βa and βc are the anodic and cathodic Tafel slopes, respectively [44]. Tafel fitting was performed over the approximately linear portions of the anodic and cathodic branches in the semi-logarithmic polarization curves. Regions exhibiting pronounced curvature or deviation from Tafel behavior, particularly near the corrosion potential and during passive-film breakdown, were excluded from the extrapolation.

The EIS spectra were fitted using equivalent electrical circuits (EECs) in ZView software to extract electrochemical parameters associated with the oxide film, pore-related response, and charge-transfer processes at the metal/electrolyte interface. Constant phase elements (CPEs) were used instead of ideal capacitors to account for surface heterogeneity and non-ideal capacitive behavior. In the EECs, R_s represents the solution resistance, while R_f, R_{pore}, R_{oxide}, and R_{ct} represent the resistances of the corrosion product film, pores, oxide layer, and charge-transfer process at the electrical double layer, respectively, depending on the specific equivalent circuit model applied. CPE_f, CPE_{pore}, CPE_{oxide}, and CPE_{dl} represent the non-ideal capacitive responses of the corrosion product film, pores, oxide layer, and double layer, respectively, while n_f, n_{pore}, n_{oxide}, and ndl describe their corresponding heterogeneity factors. C_{oxide} and C_{pore} are the ideal capacitances of the oxide layer and pores, respectively. In addition, L and R_l are the inductance and pit charge-transfer resistance, respectively [45]. Effective capacitance values were determined from the CPE parameters using the Brug relationship [46]. The CPE impedance and the corresponding effective capacitance, C_{eff}, are expressed by Equations (2) and (3), respectively [47]:

$$Z_{CPE} = 1/(Q \cdot (j \cdot \omega)^n) \quad (2)$$

$$C_{eff} = (Q \cdot R_{eq}^{1-n})^{(1/n)} \quad (3)$$

where Z_{CPE} is the CPE impedance, Q is the CPE admittance parameter, j is the imaginary unit, ω is the angular frequency (rad/s), and R_{eq} is the equivalent resistance calculated from the parallel combination of the series resistance and the resistance associated with

the considered CPE. The exponent n varies between −1 and 1: $n = 1$ corresponds to an ideal capacitor, $n = 0$ to an ideal resistor, and $n = -1$ to a pure inductor [48].

3. Results and Discussion

3.1. Microstructural and Phase Evolution of A20X Alloy Under Different Conditions

3.1.1. Microstructure of the as-Built A20X Alloy

Figure 1a shows that the as-built A20X alloy has a fine cellular microstructure with equiaxed grains (~1.23 ± 0.5 μm). This morphology is typical of LPBF aluminum alloys and results from the rapid solidification conditions of LPBF and the heterogeneous nucleation promoted by TiB_2 particles [4,6]. After FSW, the stir zone still consists of fine equiaxed grains, although the average grain size increases slightly to ~2.01 ± 0.94 μm. The limited grain coarsening is consistent with dynamic recrystallization during welding. Grain growth may also have been constrained by the short FSW thermal cycle and Zener pinning by thermally stable TiB_2 particles [10].

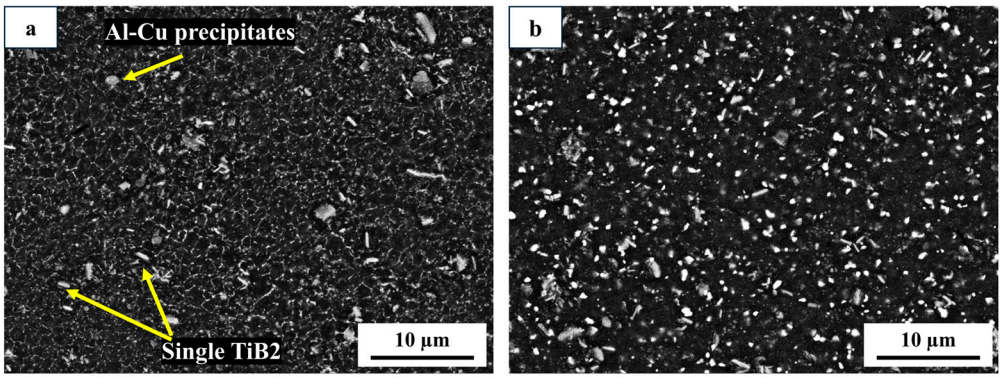


Figure 1. SEM micrographs of (**a**) the base material and (**b**) the stir zone.

3.1.2. Heat Treatment and XRD Analysis

Figure 2a shows that solution treatment (530 °C for 2.5 h) followed by aging (195 °C for 8 h) increases hardness in both the base material and stir zone regions. The BM hardness rises from 115 ± 2 to 151 ± 3 HV, while the SZ hardness increases from 125 ± 5 to 148 ± 1 HV. The higher hardness of the as-welded SZ relative to the BM may be related to the redistribution of second phases during FSW. After solution treatment and peak-aging, both regions show similar hardness levels, indicating that precipitation strengthening becomes the predominant contribution to hardness and reduces the initial difference between BM and SZ. The hardening response is attributed to the dissolution of pre-existing θ–Al_2Cu during solution treatment and the subsequent precipitation of fine θ′ and/or Ω–Al_2Cu during aging [10,11,13].

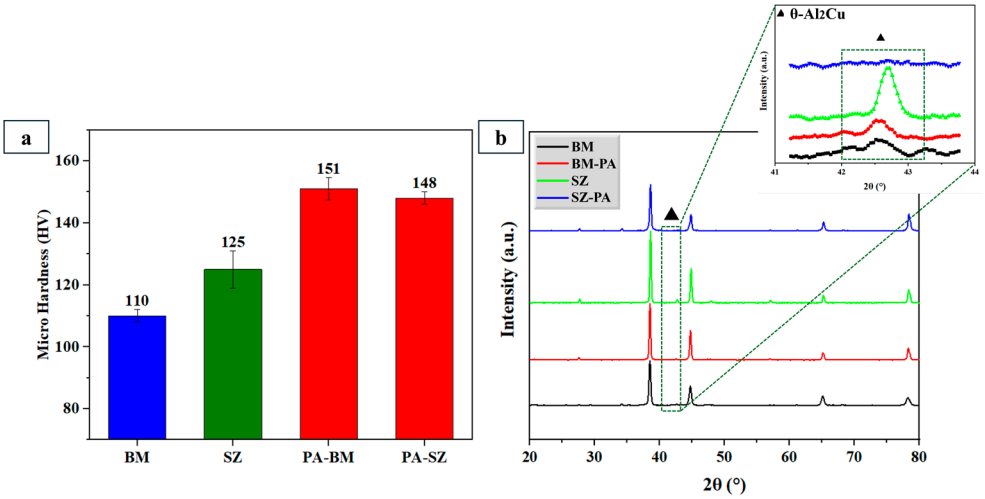


Figure 2. (**a**) Vickers microhardness and (**b**) XRD patterns of BM, SZ, BM–PA, and SZ–PA.

XRD patterns of BM, SZ, BM–PA, and SZ–PA (Figure 2b) reveal Al and TiB_2 peaks in all conditions. A magnified view around $2\theta \approx 42.5°$ indicates the presence of θ–Al_2Cu in some conditions. This peak is strongest in the as-welded SZ, and, together with the microstructural observations, may reflect a greater amount, higher crystallinity, and/or coarser θ–Al_2Cu relative to the as-built BM. The XRD result is therefore consistent with the STEM observations, which show that welding fragments the original boundary network and transforms part of it into coarser discrete precipitates.

After solution treatment and aging, a weak θ–Al_2Cu signal reappears in BM–PA, which is consistent with partial reprecipitation. By contrast, no clear θ–Al_2Cu peak is detected in SZ–PA. This result may result from the stirring action during FSW, which promotes greater chemical homogeneity and may limit the formation of relatively coarse precipitates in solute-rich areas. The absence of the θ–Al_2Cu peak in SZ–PA, however, should not be interpreted as the complete absence of Cu-containing precipitates; rather, it likely reflects their smaller size, lower volume fraction, and/or more homogeneous dispersion, which reduces XRD detectability.

3.1.3. Microstructural Evolution (STEM and TEM Analysis)

The STEM results in Figure 3 illustrate the differences in the precipitate distribution after FSW and aging among BM, SZ, and BM–PA. In the BM (Figure 3a), the grain boundaries are characterized by nearly continuous Cu- and Ag-rich films (see also Figure 4a). These boundary films arise from solute rejection during rapid LPBF solidification, which enriches the last liquid in Cu and Ag and promotes the formation of intermetallic networks [6]. Consistent with previous studies [10,11] and with the XRD data in Figure 2b, these Cu-rich constituents are mainly associated with θ–Al_2Cu. In the SZ (Figure 3b), the nearly continuous boundary network observed in BM is disrupted. This observation is consistent with fragmentation, redistribution, and possible partial dissolution of the boundary constituents during the thermomechanical cycle of FSW. The stir zone is therefore chemically more homogeneous at the mesoscale than the BM, but it also contains redistributed Cu-rich constituents that could contribute to local electrochemical heterogeneity.

Peak-aging of the base material (BM–PA) produces a further major microstructural change. The reduced presence of coarse Cu- and Ag-rich boundary constituents after solution treatment is due to their partial dissolution, while subsequent aging produces a fine intragranular dispersion of nanoscale precipitates. High-resolution TEM observations (Figure 4) confirm that these precipitates are finely distributed within the grains and

exhibit plate-like morphologies that are consistent with θ′–Al_2Cu and/or Ω–Al_2Cu phases, as inferred from their size, morphology, and distinct orientations along several habit planes [49–52]. These intragranular nanoprecipitates were not detected in the BM or SZ regions prior to heat treatment but were observed after solution treatment and peak-aging. This suggests that the applied T6 heat treatment promotes the precipitation of these metastable strengthening phases under the examined conditions. Instead, neither LPBF nor FSW alone would provide sufficient thermal activation to induce appreciable phase formation. Figure 5 provides a schematic diagram of the microstructural evolution under the various processing conditions to facilitate interpretation of the observed changes. Depending on their size and coherency, the nanoscale precipitates contribute to strengthening through lattice coherency strain and the Orowan mechanism [12]. At the same time, their refined dispersion may increase the number of electrochemically heterogeneous interfaces.

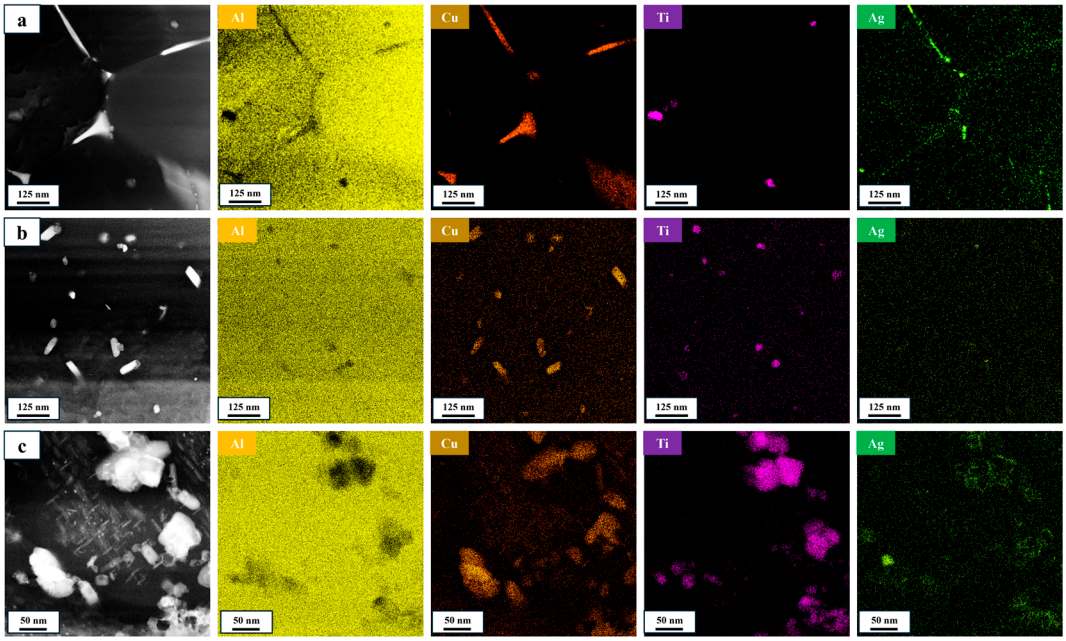


Figure 3. STEM–EDS maps showing the distribution of precipitate-forming elements in (**a**) BM, (**b**) SZ, and (**c**) BM–PA. Mg and Si were also detected and were distributed relatively homogeneously.

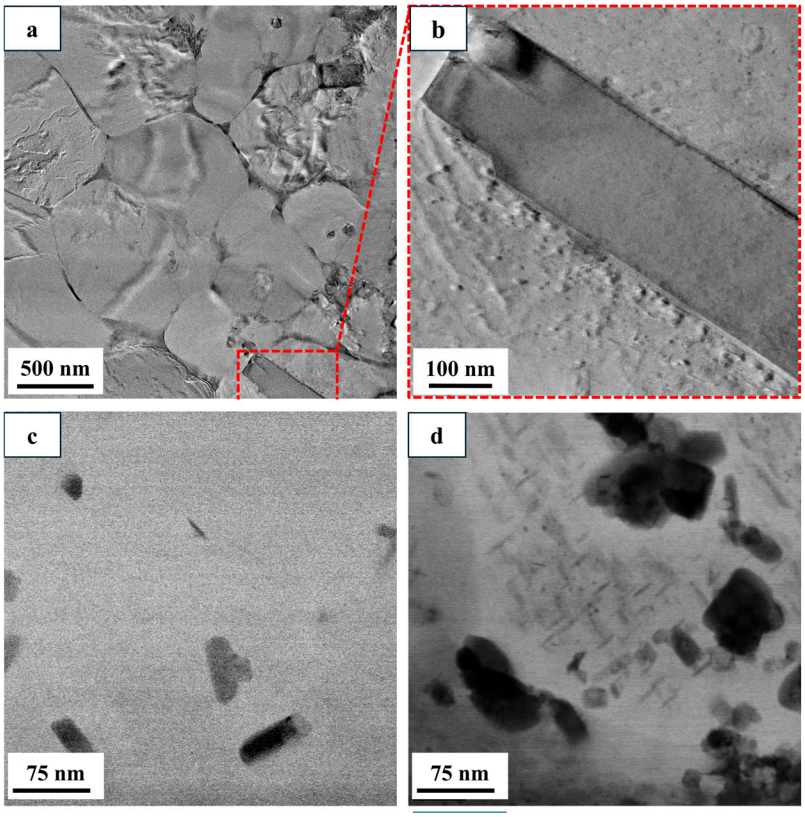


Figure 4. TEM micrographs showing the microstructure of (**a**) the BM, (**b**) a magnified view of a TiB_2 particle from (**a**), (**c**) the SZ, and (**d**) after solution treatment and peak-aging.

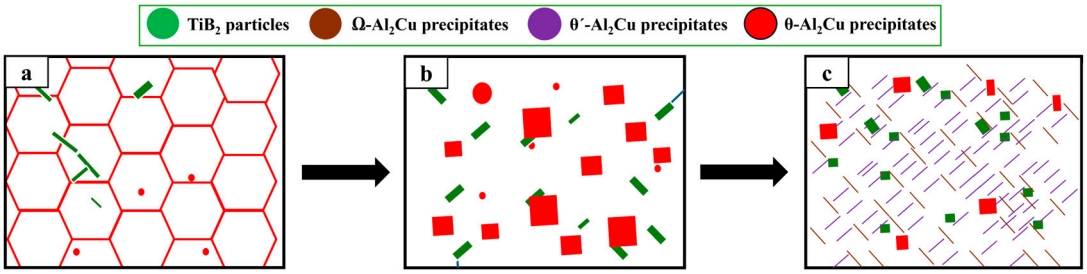


Figure 5. Schematic illustration of the microstructural evolution from (**a**) the BM to (**b**) the SZ and finally to (**c**) the peak-aged condition.

3.2. Corrosion Behavior

3.2.1. Potentiodynamic Polarization

The potentiodynamic polarization curves are depicted in Figure 6. The extracted electrochemical parameters are summarized in Table 2.

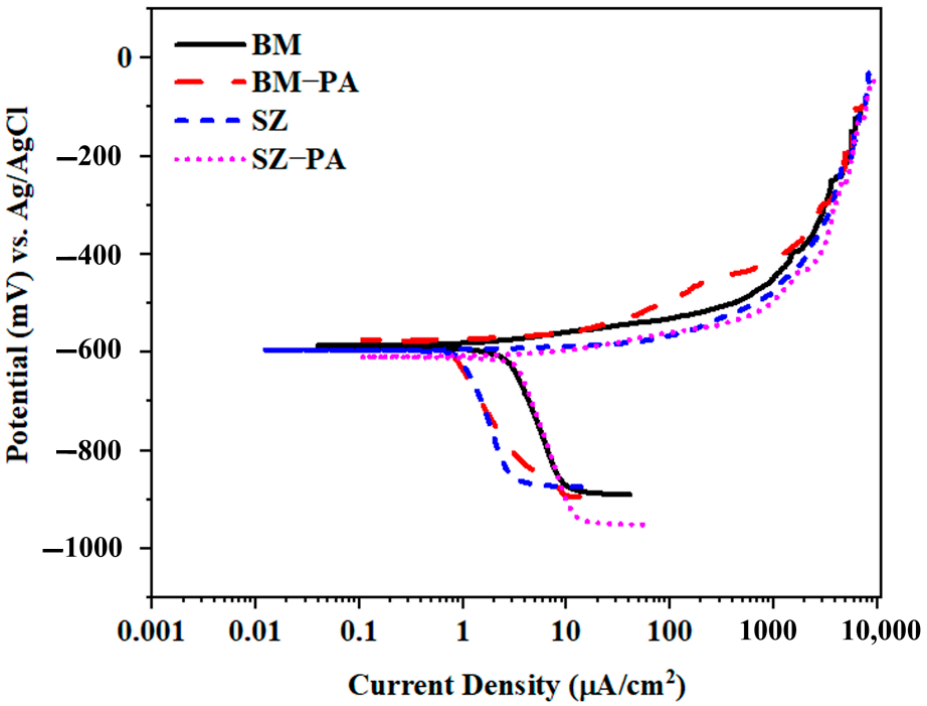


Figure 6. Potentiodynamic polarization curves for BM, SZ, BM–PA, and SZ–PA samples.

Table 2. Electrochemical parameters extracted from the polarization curves using the Tafel extrapolation method.

Sample	E_{corr} (mV)	I_{corr} (μA/cm²)	R_{pol} (kΩ·cm²)
BM	−575.5	0.703	6.605
BM–PA	−577.1	2.257	5.051
SZ	−595.4	0.966	3.544
SZ–PA	−607.4	3.181	3.519

The measured corrosion potentials of BM and BM–PA are very similar, −575.5 and −577.1 mV, whereas SZ and SZ–PA exhibit more negative values, −595.4 and −607.4 mV. These lower corrosion potential values indicate a slightly greater thermodynamic susceptibility to corrosion initiation in the SZ (in both the as-welded and peak-aged states) under the investigated exposure conditions. Because the corrosion potential (E_{corr}) is governed by the coupled anodic and cathodic reactions and does not by itself quantify the corrosion kinetics, it should be interpreted together with the corresponding corrosion current density (I_{corr}) and electrochemical impedance data. For the investigated FSW parameter set and aging schedule, I_{corr} increased from 0.703 μA/cm² for BM to 0.966 μA/cm² for SZ, 2.257 μA/cm² for BM–PA, and 3.181 μA/cm² for SZ–PA. Because one specimen was tested per condition, these differences are reported as trends rather than statistically significant effects. These findings suggest that post-weld heat treatment significantly impairs corrosion resistance of the A20X alloy than FSW alone. Broader effects of FSW parameters or heat-treatment schedules cannot be inferred from the present dataset. The effect of aging is particularly pronounced for the welded microstructure, as also reflected in the EIS response. This trend suggests that the overall corrosion response is more strongly influenced by the microstructural state rather than the small shift in corrosion potential (E_{corr}). The lowest corrosion resistance exhibited by the SZ–PA condition may be associated with redistribution and precipitation of Cu-rich constituents and changes in particle-matrix interfacial area. Specifically, the SZ–PA samples contain fine aging precipitates while the weld thermal cycle redistributed Cu-rich particles,

potentially increasing the number of cathodic sites and favoring micro-galvanic interactions. Although the occurrence of micro-galvanic coupling cannot be clearly demonstrated, the localized morphologies discussed in Section 3.2.3. are consistent with this interpretation [47].

Electrochemical parameters summarized in Table 2 reveal that I_{corr} ranges from a minimum of 0.703 μA/cm² for the BM to a maximum of 3.181 μA/cm² for SZ–PA. Under the assumptions used to convert current density to material loss, Faraday's law relates I_{corr} to an estimated corrosion rate and, hence, to degradation kinetics. Furthermore, the higher polarization resistance (R_p) measured for the BM indicates greater corrosion resistance, whereas the lower R_p of the SZ–PA condition reflects reduced resistance to corrosion.

Under the examined immersion and polarization conditions, the size, distribution, and interfacial condition of the second phases are plausible factors affecting the electrochemical response [34,53,54]. The literature data [43,55,56] show potential differences between Al-Cu precipitates, TiB_2 particles, and the Al matrix, providing a thermodynamic basis for possible local galvanic interactions. Corrosion sensitivity increases when multiple phases with different electrochemical potentials coexist, because their interfaces can behave as micro-galvanic couples [34,53]. Under the test conditions reported in the cited studies, the Al–Cu precipitates have a potential of approximately −0.695 V, whereas the aluminum matrix ranges from −0.744 to −0.854 V [55,56]. Additionally, TiB_2 particles exhibit a potential mismatch of about 0.257 V relative to aluminum [43], which can provide a driving force for micro-galvanic corrosion. In the peak-aged condition, Al–Cu precipitates increase the number of anodic–cathodic interfaces, which contributes to the highest current density observed after aging [12,57,58]. In addition, the fragmentation of TiB_2 particles after FSW can contribute to increasing the total particle-matrix interfacial area, thereby further enhancing micro-galvanic activity. This dependence on microstructure can help to explain why corrosion trends differ among literature studies. For instance, Fahimpour et al. [34] found that the welded regions in both FSW and GTAW of Al6061 exhibited lower corrosion resistance than the BM, although the FSW joints still outperformed their GTAW counterparts. Subsequent T6 heat treatment induced an anodic shift in the corrosion potential (E_{corr}) towards more positive values, and the authors reported improved corrosion resistance. This effect was more pronounced within the welded regions than in the base metal. In contrast, Nikseresht et al. [54] reported superior corrosion resistance in the GTAW weld zone of Al6061 relative to the base material. In their study, post-weld T6 heat treatment shifted the corrosion potential of the base material toward more positive values, while exerting no significant impact on the weld region itself. These differing outcomes underline that the competitive interplay among grain refinement, precipitate redistribution, defect density, and post-weld thermal history is highly sensitive to the specific processing parameters and alloy microstructures.

3.2.2. Electrochemical Impedance Spectroscopy

EIS measurements provide additional insight into the corrosion behavior of the samples under the examined material conditions. Figures 7 and 8 present the corresponding Nyquist and Bode impedance-magnitude and phase-angle plots. In the Nyquist representation, BM exhibits the largest capacitive arc and the highest low-frequency impedance magnitude, indicating the greatest overall resistance to interfacial electrochemical processes among the examined conditions. By contrast, BM–PA and SZ–PA exhibit low-frequency inductive loops that may be associated with the relaxation of adsorbed intermediates, film dissolution, repassivation, or localized pitting corrosion. BM and SZ do not exhibit a clearly resolved low-frequency inductive contribution within the investigated frequency range, which may indicate a more stable interfacial response. The

Bode phase-angle spectra (Figure 8b) exhibit broad and overlapping maxima, indicating the presence of multiple relaxation processes. However, fitting such features with overly complex equivalent circuits containing several capacitive branches may lead to mathematical overparameterization and strong correlation among fitted parameters, thereby limiting their physical interpretability. To avoid this, physically grounded streamlined circuits were adopted (Figure 9). The BM spectrum was modeled using distinct capacitive contributions nominally associated with the outer surface film, oxide layer, pores, and electrical double layer. By contrast, the SZ spectrum was represented by a two-time-constant circuit describing the surface oxide layer and charge-transfer response. Additional pore-resistance pathways were excluded because they could not be uniquely resolved from the experimental data. For the peak-aged conditions (BM–PA and SZ–PA), a low-frequency inductive element was introduced to reproduce the observed inductive response. Such behavior may be related to the relaxation of adsorbed intermediate species and/or transient film breakdown and repassivation during pitting. This interpretation is consistent with previous studies [59] and with the severe localized damage and corrosion product deposits observed by SEM after polarization.

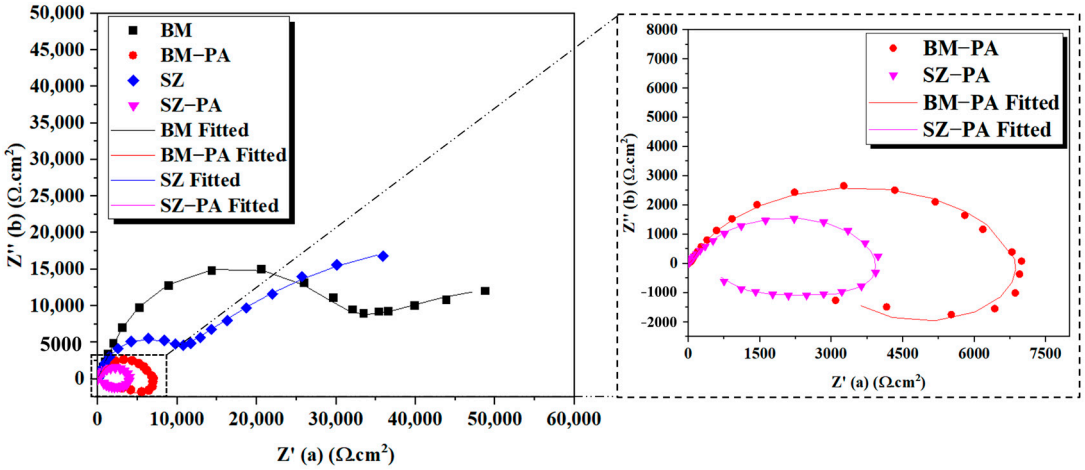


Figure 7. Nyquist plots of the EIS spectra for BM, BM–PA, SZ, and SZ–PA samples.

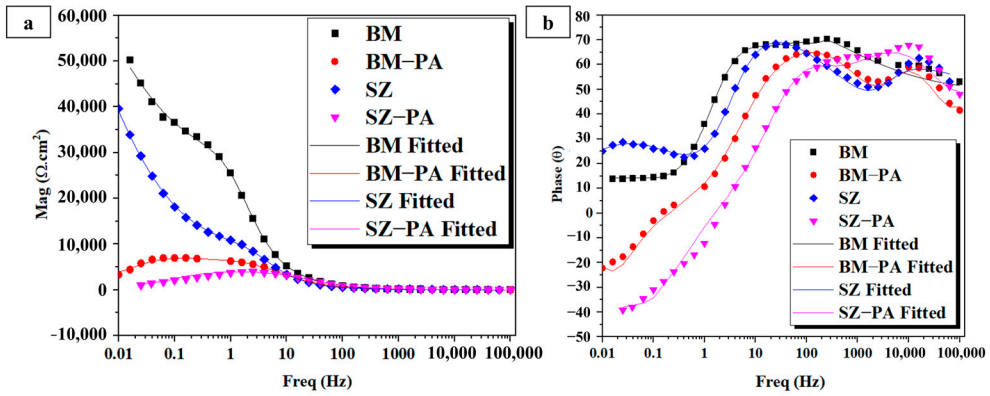


Figure 8. (**a**) Bode magnitude plots and (**b**) phase-angle plots of BM, BM–PA, SZ, and SZ–PA.

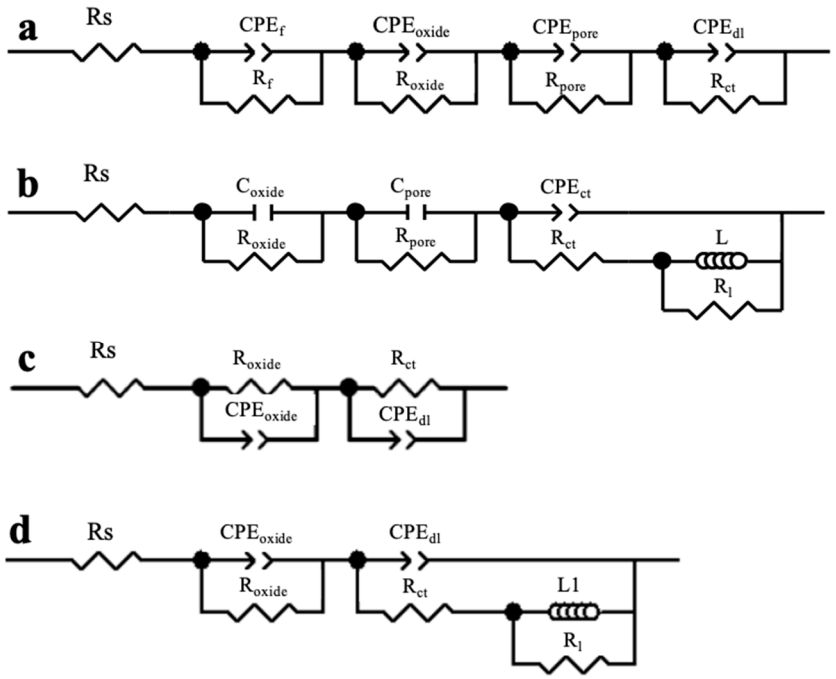


Figure 9. Equivalent electrical circuits obtained from ZView fitting for (**a**) BM, (**b**) BM–PA, (**c**) SZ, and (**d**) SZ–PA.

Based on the fitting parameters reported in Table 3, BM shows the greatest corrosion resistance, combining the highest film resistance with the largest charge-transfer resistance (R_{ct}). The charge-transfer resistance value obtained for SZ is of the same order of magnitude as that of BM, indicating that FSW alone did not substantially accelerate the interfacial electrochemical reactions. This trend is in agreement with the potentiodynamic polarization results, which showed only a moderate increase in corrosion current density before aging. Following solution treatment and peak-aging, charge-transfer resistance decreases markedly to 2946 Ω·cm² for BM–PA and 649.5 Ω·cm² for SZ–PA. These reductions, particularly the low value obtained for SZ–PA, suggest faster interfacial charge-transfer kinetics and are consistent with an increased susceptibility to localized film breakdown after heat treatment. Nevertheless, individual fitted parameters should be interpreted cautiously because they are model-dependent and may not be directly comparable among EECs with different topologies. Table 3 reports the chi-squared (χ^2) values and relative uncertainties associated with each fitted element, providing a quantitative assessment of fitting quality. Low χ^2 values and acceptable parameter uncertainties support the numerical adequacy of the selected circuits and indicate that overparameterization has been limited.

Table 3. EIS fitting parameters obtained from ZView.

Parameters	BM	Error (%)	BM–PA	Error (%)	SZ	Error (%)	SZ–PA	Error (%)
R_s (Ω·cm²)	2.96	<1	3.9	<1	6.5	Fixed	7.4	Fixed
R_f (Ω·cm²)	55,643	27.8	-	-	-	-	-	-
CPE-T_f (F/cm²)	9.96×10^{-5}	18.4	-	-	-	-	-	-
n_f	0.5	2.5	-	-	-	-	-	-
R_{oxide} (Ω·cm²)	792	67.7	35.69	8.3	7233	7.4	140.5	33.3
CPE-T_{oxide} (F/cm²)	1.14×10^{-5}	40.1	-	-	7.00×10^{-6}	10.4	4.12×10^{-6}	19.8
n_{oxide}	0.9	8.0	-	-	0.993	2.6	0.85	Fixed
C_{oxide} (μF/cm²)	-	-	1.03×10^{-6}	6.3	-	-	-	-
R_{pore} (Ω·cm²)	18.93	N/A	7.85	5.5	-	-	-	-
CPE-T_{pore} (F/cm²)	8.47×10^{-7}	N/A	-	-	-	-	-	-
n_{pore}	1.5	N/A	-	-	-	-	-	-

https://doi.org/10.3390/met16101092

R_{ct} (Ω·cm²)	26,290	7.1	2946	5.1	74,059	16.6	649.5	14.0
CPE-T_{dl} (F/cm²)	4.34×10^{-6}	7.2	8.08×10^{-6}	4.4	8.95×10^{-5}	7.5	3.74×10^{-6}	20.5
n_{dl}	0.9	4.0	0.8	0.9	0.535	1.5	0.879	4.2
L (H·cm²)	-	-	27,471	9.1	-	-	3059	8.8
R_l (Ω·cm²)	-	-	4030	3.8	-	-	2888	4.8
Chi-Squared (χ^2)	0.0058	-	0.0047	-	0.0097	-	0.0294	-

3.2.3. SEM/EDS Analysis of Corroded Surfaces

SEM examination of the post-polarization surfaces (Figure 10) reveals localized cavities and associated deposits that are morphologically consistent with pitting in all examined conditions. The representative micrographs show qualitative differences in the apparent extent and morphology of the localized damage. BM shows relatively fewer and less developed pits, whereas BM–PA and especially SZ–PA exhibit extensive damaged regions and accumulations of corrosion products around the pits. These observations agree with the ordering suggested by the polarization and EIS results, particularly for SZ–PA: the peak-aged conditions exhibit more extensive dissolution and greater accumulation of corrosion products around or inside the pits. Therefore, SEM evidence supports an association between the solution-treatment and aging cycle and more extensive localized post-polarization damage, especially in the welded condition.

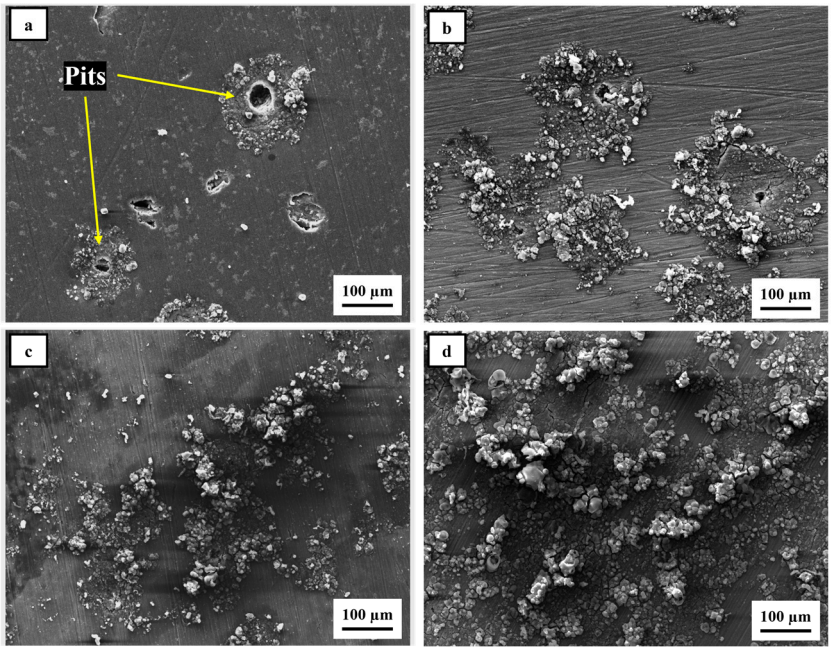


Figure 10. SEM images of the sample surfaces after the potentiodynamic polarization test: (**a**) BM, (**b**) SZ, (**c**) BM–PA, and (**d**) SZ–PA.

EDS point analyses were performed at the selected locations shown in Figure 11. The EDS spectra indicate the predominant presence of Al and O, with smaller amounts of Cl, Ti, and Cu. The Al and O signals are consistent with oxygen-containing corrosion products; however, EDS cannot distinguish among Al_2O_3, $Al(OH)_3$, aluminum oxyhydroxides, or other oxygen-containing phases. The Ti and Cu signals observed at or near the pit zones are consistent with a possible contribution to micro-galvanic coupling and, hence, to the preferential dissolution of the surrounding Al matrix. The detection of Cl in the post-polarization EDS spectra indicates the presence of chlorine-containing species on the corroded surface. This observation alone does not clearly establish the role of chloride in the corrosion mechanism. The apparent discrepancy between the EIS evidence of film formation and the post-test damage observed by SEM is not necessarily

contradictory. Instead, it reflects the transient nature of the passive layer in chloride solution, which may undergo dynamic cycles of localized breakdown and repassivation during active localized attack [60,61].

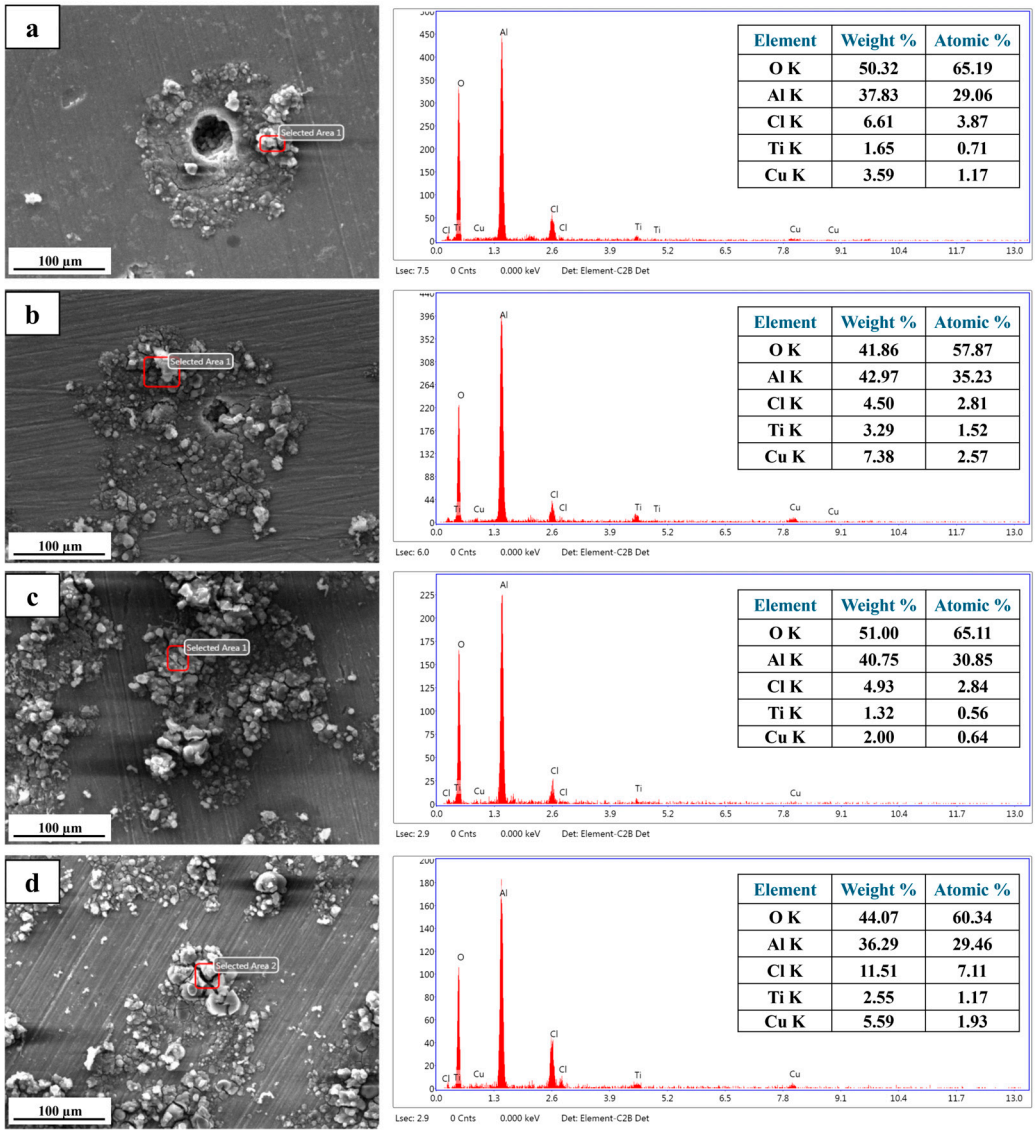


Figure 11. Representative SEM images and corresponding EDS analysis performed on the marked locations from the corroded surfaces after the potentiodynamic polarization test: (**a**) BM, (**b**) SZ, (**c**) BM–PA, and (**d**) SZ–PA.

4. Conclusions

This study investigates the corrosion behavior of LPBF A20X under the selected FSW and post-weld heat-treatment conditions. Under the investigated conditions and based on the microstructural and electrochemical analyses, the main conclusions are as follows:

1. BM exhibited the lowest corrosion current density and the highest low-frequency impedance, whereas SZ–PA showed the highest corrosion current density and the most extensive post-polarization damage.
2. FSW alone was associated with a smaller increase in the estimated corrosion current density relative to BM, while the solution-treatment and aging cycle was associated with a substantially greater increase, especially when combined with the welded microstructure.

3. The combined STEM/TEM, SEM/EDS, XRD, and electrochemical observations are consistent with a possible contribution from micro-galvanic interactions involving the Al matrix, Cu-rich constituents, and TiB_2 particles.
4. Solution treatment and peak-aging were associated with lower low-frequency impedance, inductive behavior, and more extensive post-polarization damage consistent with pitting, particularly in SZ–PA.

Overall, these findings highlight the need to optimize post-weld heat-treatment conditions for LPBF A20X by balancing precipitation strengthening against susceptibility to localized corrosion in friction stir welded components.

Author Contributions: Conceptualization: M.A. and P.R.S.; methodology: M.A. and P.R.S.; formal analysis and investigation: M.A., P.R.S. and P.M.; writing—review and editing: M.A., P.R.S. and P.M.; visualization: M.A.; supervision: P.R.S.; project administration: P.R.S.; funding acquisition: P.M. and P.R.S. All authors have read and agreed to the published version of the manuscript.

Funding: This study was carried out within the Space It Up project funded by the Italian Space Agency, ASI, and the Italian Ministry of University and Research, MUR, under contract n. 2024–5–E.0–CUP n. I53D24000060005.

Data Availability Statement: The data supporting the findings of this study are available from the corresponding author upon reasonable request.

Conflicts of Interest: The authors declare no conflicts of interest.

References

1. Avateffazeli, M.; Khan, M.F.; Shamsaei, N.; Haghshenas, M. Microstructure, Mechanical, and Fatigue Properties of a Laser Powder Bed Fused Al-Cu-Mg-Ag-Ti-B (A205) Alloy. In Proceedings of the 2022 International Solid Freeform Fabrication Symposium, Austin, TX, USA, 25–27 July 2022. https://doi.org/10.26153/TSW/44159.https://repositories.lib.utexas.edu/items/14c9fc15-a040-428b-a28e-55b64385c4df
2. Avateffazeli, M.; Shakil, S.I.; Hadadzadeh, A.; Shalchi-Amirkhiz, B.; Pirgazi, H.; Mohammadi, M.; Haghshenas, M. On Microstructure and Work Hardening Behavior of Laser Powder Bed Fused Al-Cu-Mg-Ag-TiB2 and AlSi10Mg Alloys. *Mater. Today Commun.* **2023**, *35*, 105804. https://doi.org/10.1016/J.MTCOMM.2023.105804.
3. Karimialavijeh, H.; Ghasri-Khouzani, M.; Chakraborty, A.; Pröbstle, M.; Martin, E. Direct Aging of Additively Manufactured A20X Aluminum Alloy. *J. Alloys Compd.* **2023**, *968*, 172071. https://doi.org/10.1016/J.JALLCOM.2023.172071.
4. Ghasri-Khouzani, M.; Karimialavijeh, H.; Pröbstle, M.; Batmaz, R.; Muhammad, W.; Chakraborty, A.; Sabiston, T.D.; Harvey, J.P.; Martin Processability and Characterization of A20X Aluminum Alloy Fabricated by Laser Powder Bed Fusion. *Mater. Today Commun.* **2023**, *35*, 105555. https://doi.org/10.1016/J.MTCOMM.2023.105555.
5. Shakil, S.I.; Beamer, C.; Attallah, M.M.; Haghshenas, M. The Effect of Heat Treatment on Local Mechanical Properties of Laser Powder Bed Fused and Hot Isostatically Pressed Al-Cu-Mg-Ag-TiB2 (A20X) Aluminum Alloy. *JOM* **2024**, *76*, 31–41. https://doi.org/10.1007/S11837-023-06233-3.
6. Ghoncheh, M.H.; Sanjari, M.; Zoeram, A.S.; Cyr, E.; Amirkhiz, B.S.; Lloyd, A.; Haghshenas, M.; Mohammadi, M. On the Microstructure and Solidification Behavior of New Generation Additively Manufactured Al-Cu-Mg-Ag-Ti-B Alloys. *Addit. Manuf.* **2021**, *37*, 101724. https://doi.org/10.1016/J.ADDMA.2020.101724.
7. Biffi, C.A.; Bassani, P.; Fiocchi, J.; Albu, M.; Tuissi, A. Selective Laser Melting of AlCu-TiB2 Alloy Using Pulsed Wave Laser Emission Mode: Processability, Microstructure and Mechanical Properties. *Mater. Des.* **2021**, *204*, 109628. https://doi.org/10.1016/J.MATDES.2021.109628.
8. Li, S.; Cai, B.; Duan, R.; Tang, L.; Song, Z.; White, D.; Magdysyuk, O.V.; Attallah, M.M. Synchrotron Characterisation of Ultra-Fine Grain TiB2/Al-Cu Composite Fabricated by Laser Powder Bed Fusion. *Acta Metall. Sin. (Engl. Lett.)* **2022**, *35*, 78–92. https://doi.org/10.1007/S40195-021-01317-Y.
9. Mair, P.; Kaserer, L.; Braun, J.; Weinberger, N.; Letofsky-Papst, I.; Leichtfried, G. Microstructure and Mechanical Properties of a TiB2-Modified Al–Cu Alloy Processed by Laser Powder-Bed Fusion. *Mater. Sci. Eng. A* **2021**, *799*, 140209. https://doi.org/10.1016/J.MSEA.2020.140209.

10. Avateffazeli, M.; Carrion, P.E.; Shachi-Amirkhiz, B.; Pirgazi, H.; Mohammadi, M.; Shamsaei, N.; Haghshenas, M. Correlation between Tensile Properties, Microstructure, and Processing Routes of an Al–Cu–Mg–Ag–TiB2 (A205) Alloy: Additive Manufacturing and Casting. *Mater. Sci. Eng. A* **2022**, *841*, 142989. https://doi.org/10.1016/J.MSEA.2022.142989.
11. Barode, J.; Vayyala, A.; Virgillito, E.; Aversa, A.; Mayer, J.; Fino, P.; Lombardi, M. Revisiting Heat Treatments for Additive Manufactured Parts: A Case Study of A20X Alloy. *Mater. Des.* **2023**, *225*, 111566. https://doi.org/10.1016/J.MATDES.2022.111566.
12. Karimialavijeh, H.; Chakraborty, A.; Azzi, M.; Proebstle, M.; Martin, E. Effect of Precipitation Hardening on the Microstructure, Mechanical, and Corrosion Properties of Additively Manufactured A20X Aluminum Alloy. *Mater. Sci. Eng. A* **2024**, *913*, 147033. https://doi.org/10.1016/J.MSEA.2024.147033.
13. Shakil, S.I.; Zoeram, A.S.; Pirgazi, H.; Shalchi-Amirkhiz, B.; Poorganji, B.; Mohammadi, M.; Haghshenas, M. Microstructural-Micromechanical Correlation in an Al–Cu–Mg–Ag–TiB2 (A205) Alloy: Additively Manufactured and Cast. *Mater. Sci. Eng. A* **2022**, *832*, 142453. https://doi.org/10.1016/J.MSEA.2021.142453.
14. Abankar, M.; Lunetto, V.; De Maddis, M.; Russo Spena, P. Friction Stir Welding of Additively Manufactured A20X Aluminum Alloy: Welding Process, Mechanical Properties, and Microstructure. *Int. J. Adv. Manuf. Technol.* **2024**, *135*, 4635–4652. https://doi.org/10.1007/S00170-024-14747-6.
15. Abankar, M.; Lunetto, V.; De Maddis, M.; Lombardi, F.; Razza, V.; Spena, P.R. Friction Stir Welding of Laser-Powder Bed Fusion Manufactured A20X. *Period. Polytech. Mech. Eng.* **2024**, *68*, 346–351. https://doi.org/10.3311/PPME.38444.
16. Prashanth, K.G.; Damodaram, R.; Scudino, S.; Wang, Z.; Prasad Rao, K.; Eckert, J. Friction Welding of Al–12Si Parts Produced by Selective Laser Melting. *Mater. Des.* **2014**, *57*, 632–637. https://doi.org/10.1016/J.MATDES.2014.01.026.
17. Moeini, G.; Sajadifar, S.V.; Wegener, T.; Rössler, C.; Gerber, A.; Böhm, S.; Niendorf, T. On the Influence of Build Orientation on Properties of Friction Stir Welded Al–Si10Mg Parts Produced by Selective Laser Melting. *J. Mater. Res. Technol.* **2021**, *12*, 1446–1460. https://doi.org/10.1016/J.JMRT.2021.03.101.
18. Moeini, G.; Sajadifar, S.V.; Wegener, T.; Brenne, F.; Niendorf, T.; Böhm, S. On the Low-Cycle Fatigue Behavior of Friction Stir Welded Al–Si12 Parts Produced by Selective Laser Melting. *Mater. Sci. Eng. A* **2019**, *764*, 138189. https://doi.org/10.1016/J.MSEA.2019.138189.
19. Abankar, M.; Lunetto, V.; Russo Spena, P. Friction Stir Welding of Additively Manufactured CuNiSiCr: Effect of Post-Weld Heat Treatments on Microstructure and Mechanical Properties. *Int. J. Adv. Manuf. Technol.* **2025**, *141*, 5429–5445. https://doi.org/10.1007/S00170-025-16924-7.
20. Ahmed, M.M.Z.; El-Sayed Seleman, M.M.; Fydrych, D.; Çam, G. Review on Friction Stir Welding of Dissimilar Magnesium and Aluminum Alloys: Scientometric Analysis and Strategies for Achieving High-Quality Joints. *J. Magnes. Alloys* **2023**, *11*, 4082–4127. https://doi.org/10.1016/J.JMA.2023.09.039.
21. Abdul Khaliq, U.; Muhamad, M.R.; Yusof, F.; Ibrahim, S.; Mohd Isa, M.S.; Chen, Z.; Çam, G. A Review on Friction Stir Butt Welding of Aluminum with Magnesium: A New Insight on Joining Mechanisms by Interfacial Enhancement. *J. Mater. Res. Technol.* **2023**, *27*, 4595–4624. https://doi.org/10.1016/J.JMRT.2023.10.158.
22. Laska, A.; Szkodo, M.; Cavaliere, P.; Moszczyńska, D.; Mizera, J. Analysis of Residual Stresses and Dislocation Density of AA6082 Butt Welds Produced by Friction Sir Welding. *Metall. Mater. Trans. A* **2022**, *54*, 211–225. https://doi.org/10.1007/S11661-022-06862-4.
23. Çam, G.; Javaheri, V.; Heidarzadeh, A. Advances in FSW and FSSW of Dissimilar Al-Alloy Plates. *J. Adhes. Sci. Technol.* **2023**, *37*, 162–194. https://doi.org/10.1080/01694243.2022.2028073
24. Mirandola, P.; Novel, D.; Perini, M.; Benedetti, M.; Lombardi, F.; Lunetto, V.; Spena, P.R. Microstructures and Mechanical Properties of Friction Stir Welded Additively Manufactured Scalmalloy®. *Int. J. Adv. Manuf. Technol.* **2024**, *134*, 1645–1660. https://doi.org/10.1007/S00170-024-14237-9
25. Miao, H.; Qiu, Z.; He, D.; Xue, F.; Xiao, L.; Ding, S. Precipitation Evolution and Mechanical Response of 2219 Aluminum Alloy FSW Joints Under Electromagnetic Induction Heating Pulsed Aging. *Metall. Mater. Trans. A* **2026**, *57*, 2687–2700. https://doi.org/10.1007/S11661-026-08194-Z.
26. Scherillo, F.; Astarita, A.; Prisco, U.; Contaldi, V.; di Petta, P.; Langella, A.; Squillace, A. Friction Stir Welding of AlSi10Mg Plates Produced by Selective Laser Melting. *Metallogr. Microstruct. Anal.* **2018**, *7*, 457–463. https://doi.org/10.1007/S13632-018-0465-Y.
27. Mirandola, P.; Lunetto, V.; Novel, D.; Barozzi, M.; Bellutti, P.; De Maddis, M.; Russo Spena, P. Strength and Microstructure of Friction Stir Welded Additively Manufactured Scalmalloy® in As-Welded and Heat-Treated Conditions. *J. Manuf. Process.* **2023**, *97*, 1–11. https://doi.org/10.1016/J.JMAPRO.2023.04.051.
28. Abankar, M.; Lunetto, V.; Matteis, P.; Russo Spena, P. Friction Stir Welding of Additively Manufactured A20X and Effects of Post-Weld Heat Treatments. *Int. J. Adv. Manuf. Technol.* **2026**, *144*, 7953–7968. https://doi.org/10.1007/S00170-026-18315-Y.

29. Zhang, C.; Huang, G.; Liu, Q. Research on Local Corrosion Behavior of Thermo-Mechanically Affected Zone in Dissimilar AA2024/7075 Friction Stir Welds. *Intermetallics* **2021**, *130*, 107081. https://doi.org/10.1016/J.INTERMET.2020.107081.
30. Zhang, C.; Huang, G.; Cao, Y.; Zhu, Y.; Huang, X.; Zhou, Y.; Li, Q.; Zeng, Q.; Liu, Q. Microstructure Evolution of Thermo-Mechanically Affected Zone in Dissimilar AA2024/7075 Joint Produced by Friction Stir Welding. *Vacuum* **2020**, *179*, 109515. https://doi.org/10.1016/J.VACUUM.2020.109515.
31. Jamshidi Aval, H. Effect of Heat Input in Dissimilar Friction Stir Welding of A390-10 Wt.% SiC Composite–AA2024 Aluminum Alloy. *Arch. Civ. Mech. Eng.* **2024**, *24*, 172. https://doi.org/10.1007/S43452-024-00957-Y.
32. Jamshidi Aval, H.; Galvão, I. Characterization of Friction Stir Welded Al-4Cu-Mg Alloy/Al-16Si-4Cu-10SiC Composite Joint. *J. Adv. Join. Process.* **2024**, *9*, 100192. https://doi.org/10.1016/J.JAJP.2024.100192.
33. Kureshi, A.; Sudeep Kumar, T.; Sourav, A.; Verma, A.; Shanmugasundaram, T. Comparison of Corrosion Behavior of High Strength Aluminum Alloy Welded Using Various Fusion and Solid-State Welding Processes. *Weld. Int.* **2025**, *39*, 489–498. https://doi.org/10.1080/09507116.2025.2498580
34. Fahimpour, V.; Sadrnezhaad, S.K.; Karimzadeh, F. Corrosion Behavior of Aluminum 6061 Alloy Joined by Friction Stir Welding and Gas Tungsten Arc Welding Methods. *Mater. Des.* **2012**, *39*, 329–333. https://doi.org/10.1016/J.MATDES.2012.02.043.
35. Gharavi, F.; Matori, K.A.; Yunus, R.; Othman, N.K.; Fadaeifard, F. Corrosion Behavior of Al6061 Alloy Weldment Produced by Friction Stir Welding Process. *J. Mater. Res. Technol.* **2015**, *4*, 314–322. https://doi.org/10.1016/J.JMRT.2015.01.007.
36. Wei, B.; Niu, M.; Cai, Z.; Xu, J.; Sun, C.; Wang, W.; Sun, Z.; Wu, T.; Ramamurty, U. Cu-Rich Nano Precipitates Simultaneously Enhance the Tensile Properties, Antibacterial Efficacy, and Corrosion Resistance of Ultra-High Strength Steel. *Acta Mater.* **2025**, *292*, 121026. https://doi.org/10.1016/J.ACTAMAT.2025.121026.
37. Adjei-Kyeremeh, F.; Pratesa, Y.; Shen, X.; Song, W.; Raffeis, I.; Vroomen, U.; Zander, D.; Bührig-Polaczek, A. Preheating Influence on the Precipitation Microstructure, Mechanical and Corrosive Properties of Additively Built Al–Cu–Li Alloy Contrasted with Conventional (T83) Alloy. *Materials* **2023**, *16*, 4916. https://doi.org/10.3390/MA16144916.
38. Mao, Y.; Zhu, Y.; Deng, C.M.; Sun, S.; Xia, D.H. Analysis of Localized Corrosion Mechanism of 2024 Aluminum Alloy at a Simulated Marine Splash Zone. *Eng. Fail. Anal.* **2022**, *142*, 106759. https://doi.org/10.1016/J.ENGFAILANAL.2022.106759.
39. Sun, S.; Zheng, Q.; Li, D.; Hu, S.; Wen, J. Exfoliation Corrosion of Extruded 2024-T4 in the Coastal Environments in China. *Corros. Sci.* **2011**, *53*, 2527–2538. https://doi.org/10.1016/J.CORSCI.2011.04.010.
40. Zhang, S.; Zhang, T.; He, Y.; Feng, Y.; Du, X.; Ma, B.; Zhang, T. Effect of Coastal Atmospheric Corrosion on Fatigue Properties of 2024-T4 Aluminum Alloy Structures. *J. Alloys Compd.* **2019**, *802*, 511–521. https://doi.org/10.1016/J.JALLCOM.2019.06.235.
41. *ISO 4957:2018*; Tool Steels. ISO: Geneva, Switzerland, 2018. Available online: https://www.iso.org/standard/70646.html (accessed on 5 November 2025).
42. *ISO 6507-1:2023*; Metallic Materials—Vickers Hardness Test—Part 1: Test Method. ISO: Geneva, Switzerland, 2023. Available online: https://www.iso.org/standard/83898.html (accessed on 18 September 2026).
43. Rafieazad, M.; Fathi, P.; Nasiri, A.; Haghshenas, M.; Mohammadi, M. Isotropic Corrosion Performance of the Newly Developed L-PBF-A205 Aluminum Alloy. *Mater. Lett.* **2021**, *291*, 129541. https://doi.org/10.1016/J.MATLET.2021.129541.
44. Aslam, R. Potentiodynamic Polarization Methods for Corrosion Measurement. In *Electrochemical and Analytical Techniques for Sustainable Corrosion Monitoring: Advances, Challenges and Opportunities*; Elsevier: Amsterdam, The Netherlands, 2023; pp. 25–37. https://doi.org/10.1016/B978-0-443-15783-7.00003-7.
45. Taghian, M.; Heydarian, M.; Torkian, S.; Dabir, M.P.; Bahrami, A.; Mousavi Anijdan, S.H.; Park, N. High-Velocity Oxy-Fuel (HVOF) Spray Coating of Inconel, Colmonoy, and Aluminum on AISI 316L Stainless Steel: A Comparative Investigation of the Microstructure and Corrosion Resistance of Coatings. *Coatings* **2023**, *13*, 204. https://doi.org/10.3390/COATINGS13010204.
46. Brug, G.J.; van den Eeden, A.L.G.; Sluyters-Rehbach, M.; Sluyters, J.H. The Analysis of Electrode Impedances Complicated by the Presence of a Constant Phase Element. *J. Electroanal. Chem. Interfacial Electrochem.* **1984**, *176*, 275–295. https://doi.org/10.1016/S0022-0728(84)80324-1.
47. Stansbury, E.E.; Buchanan, R.A. *Fundamentals of Electrochemical Corrosion*; ASM International: Materials Park, OH, USA, 2000; p. 487.
48. Gai, X.; Bai, Y.; Li, J.; Li, S.; Hou, W.; Hao, Y.; Zhang, X.; Yang, R.; Misra, R.D.K. Electrochemical Behaviour of Passive Film Formed on the Surface of Ti-6Al-4V Alloys Fabricated by Electron Beam Melting. *Corros. Sci.* **2018**, *145*, 80–89. https://doi.org/10.1016/J.CORSCI.2018.09.010.
49. Cao, B.; Shaeffer, M.; Cadel, D.; Ramesh, K.T.; Prasad, S. An Analysis of Strengthening Mechanisms and Rate-Dependence in a High Strength Aluminum Alloy. *J. Dyn. Behav. Mater.* **2017**, *4*, 6–17. https://doi.org/10.1007/s40870-017-0136-0.

50. Gazizov, M.; Zuiko, I.; Kaibyshev, R. Effect of Plastic Deformation on a Dispersion of Omega-Phase and Mechanical Properties of an Al-Cu-Mg-Ag Alloy. *Adv. Mat. Res.* **2014**, *922*, 189–194. https://doi.org/10.4028/www.scientific.net/AMR.922.189.
51. Bai, S.; Zhou, X.; Liu, Z.; Ying, P.; Liu, M.; Zeng, S. Atom Probe Tomography Study of Mg-Dependent Precipitation of Ω Phase in Initial Aged Al-Cu–Mg–Ag Alloys. *Mater. Sci. Eng. A* **2015**, *637*, 183–188. https://doi.org/10.1016/j.msea.2015.04.052.
52. Li, Y.; Liu, Z.; Bai, S.; Zhou, X.; Wang, H.; Zeng, S. Enhanced Mechanical Properties in an Al–Cu–Mg–Ag Alloy by Duplex Aging. *Mater. Sci. Eng. A* **2011**, *528*, 8060–8064. https://doi.org/10.1016/j.msea.2011.07.055.
53. Tang, C.H.; Cheng, F.T.; Man, H.C. Effect of Laser Surface Melting on the Corrosion and Cavitation Erosion Behaviors of a Manganese–Nickel–Aluminium Bronze. *Mater. Sci. Eng. A* **2004**, *373*, 195–203. https://doi.org/10.1016/J.MSEA.2004.01.016.
54. Nikseresht, Z.; Karimzadeh, F.; Golozar, M.A.; Heidarbeigy, M. Effect of Heat Treatment on Microstructure and Corrosion Behavior of Al6061 Alloy Weldment. *Mater. Des. (1980–2015)* **2010**, *31*, 2643–2648. https://doi.org/10.1016/J.MATDES.2009.12.001.
55. Li, J.; Dang, J. A Summary of Corrosion Properties of Al-Rich Solid Solution and Secondary Phase Particles in Al Alloys. *Metals* **2017**, *7*, 84. https://doi.org/10.3390/MET7030084.
56. Muller, I.L.; Galvele, J.R. Pitting Potential of High Purity Binary Aluminium Alloys—I. Al—Cu Alloys. Pitting and Intergranular Corrosion. *Corros. Sci.* **1977**, *17*, 179–193. https://doi.org/10.1016/0010-938X(77)90044-0.
57. Scully, J.R.; Peebles, D.E.; Romig, A.D.; Frear, D.R.; Hills, C.R. Metallurgical Factors Influencing the Corrosion of Aluminum, Al-Cu, and Al-Si Alloy Thin Films in Dilute Hydrofluoric Solution. *Metall. Trans. A* **1992**, *23*, 2641–2655. https://doi.org/10.1007/BF02658068.
58. Li, J.F.; Ziqiao, Z.; Na, J.; Chengyu, T. Localized Corrosion Mechanism of 2×××-Series Al Alloy Containing S(Al2CuMg) and θ′(Al2Cu) Precipitates in 4.0% NaCl Solution at PH 6.1. *Mater. Chem. Phys.* **2005**, *91*, 325–329. https://doi.org/10.1016/J.MATCHEMPHYS.2004.11.034.
59. Öteyaka, M.Ö.; Ayrtüre, H. A Study on the Corrosion Behavior in Sea Water of Welds Aluminum Alloy by Shielded Metal Arc Welding, Friction Stir Welding and Gas Tungsten Arc Welding. *Int. J. Electrochem. Sci.* **2015**, *10*, 8549–8557. https://doi.org/10.1016/S1452-3981(23)11118-7.
60. Kim, M.M.; Kapun, B.; Tiringer, U.; Šekularac, G.; Milošev, I. Protection of Aluminum Alloy 3003 in Sodium Chloride and Simulated Acid Rain Solutions by Commercial Conversion Coatings Containing Zr and Cr. *Coatings* **2019**, *9*, 563. https://doi.org/10.3390/COATINGS9090563.
61. Mazhar, A.A.; Arab, S.T.; Noor, E.A. The Role of Chloride Ions and PH in the Corrosion and Pitting of Al-Si Alloys. *J. Appl. Electrochem.* **2001**, *31*, 1131–1140. https://doi.org/10.1023/A:1012039804089.

Disclaimer/Publisher's Note: The statements, opinions and data contained in all publications are solely those of the individual author(s) and contributor(s) and not of MDPI and/or the editor(s). MDPI and/or the editor(s) disclaim responsibility for any injury to people or property resulting from any ideas, methods, instructions or products referred to in the content.